DOI: http://dx.doi.org/10.1016/j.compstruct.2013.03.014

An experimental investigation into localised low-velocity impact loading on glass fibre-reinforced polyamide automotive product

Zakaria Mouti[1], Keith Westwood[2], Darren Long[2] and James Njuguna[1*]

[1] Centre for Automotive Technology, Department of Sustainable Systems, Cranfield University, Bedfordshire, MK43 0AL, UK, z.mouti@cranfield.ac.uk

[2] Eaton, Automotive Group, West Midlands, DY5 2LB, UK, keithwestwood@eaton.com

* Author to whom correspondence should be addressed.
Email: j.njuguna@cranfield.ac.uk,
Tel: +44-1234-75-4186, Fax: +44-1234-75-1671

1. Introduction

The under carriage of any road going production vehicle contains many vulnerability components. Driving on gravel surfaces, tough roads, near construction sites or during road maintenance can cause stones to be ejected from the wheels which then are projected into the air and could possibly damage the under carriage area of a vehicle or the vehicle can hit a boulder with potential serious consequences on low-fitted components. The main concern of this research is the impact performance and damage caused by those stones to a recently converted engine oil pan for light utility vehicles into PA66 reinforced with 35% of short glass fibre. Figure 1 shows an early version of the thermoplastic oil pan that has being damaged by foreign flying debris, identified as a stone by the fragments left on the impacted surface (Figure 1-a). The engine oil was seeping out through the crack from the inner side (Figure 1-b) to the outer side of the pan (Figure 1-a).

Damage tolerant design of vehicle components requires a methodology to predict the likelihood of critical impacts occurring over the operational lifetime of the vehicle. Such information could be provided by examination of the damage caused in previous incidents, so that the locations of severe impact damage can be mapped out. In practice, the limited availability of such detailed records makes this approach very difficult to utilise. An alternative approach relies on understanding the complex lofting processes of objects by wheels, which may be considered as an impact event given the high speed at which a tyre may contact the object [1].

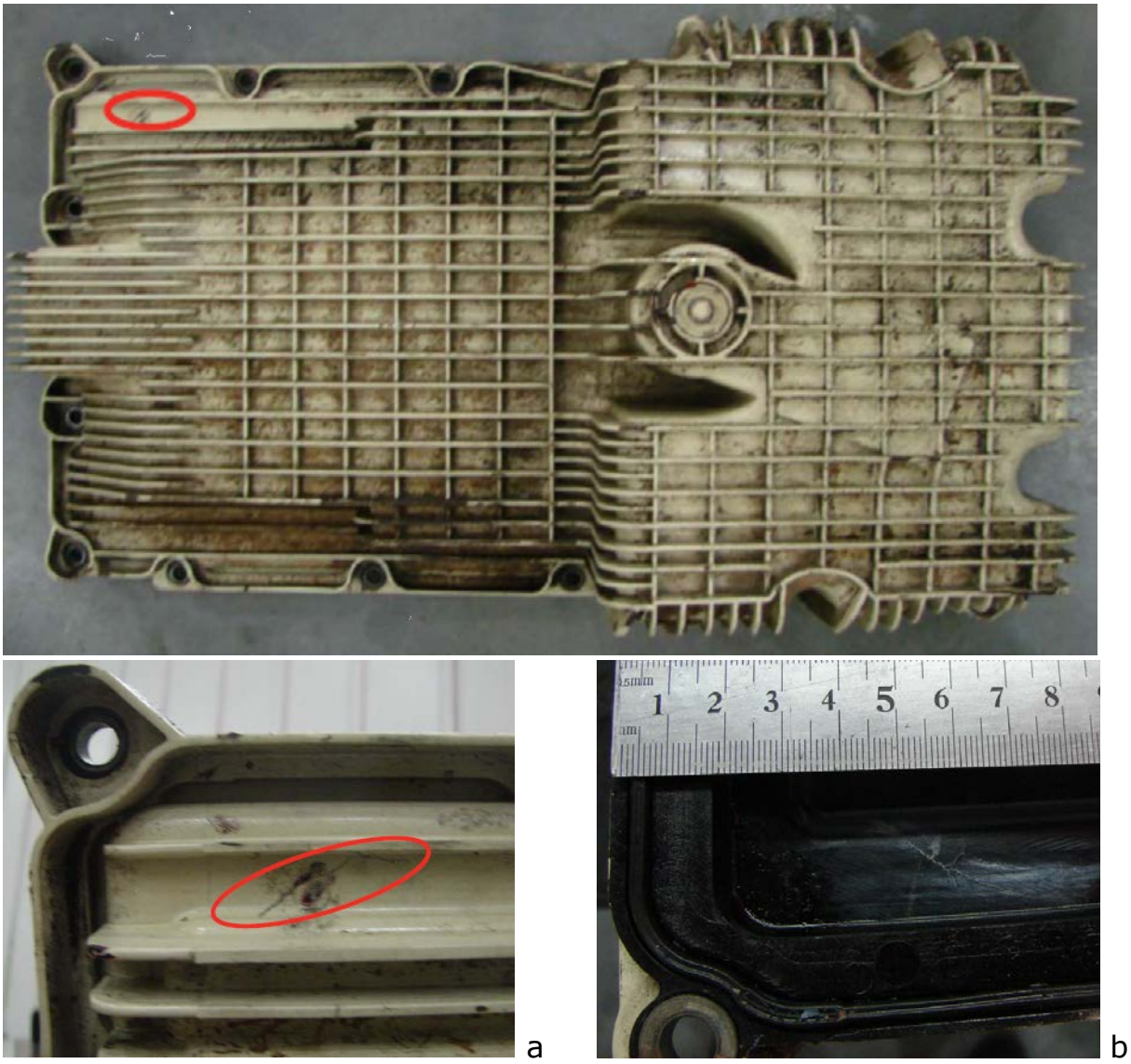

a b

Figure 1 - Thermoplastic oil pan crack failure, a) outer side, b) inner side [2]

A number of investigations were conducted to assess the threat of impact damage caused to vehicles or aircrafts by tyre-lofted runway debris, yet there is limited understanding in the stone lofting process and in the influence of stone characteristics [3; 1; 4-7]. It comes out that a compilation of stones collected from roads or airfields led to stones of various shape with different overlaps, orientations and densities. However, the conditions most conducive to stone lifting concerns stones with small diameters lofted following four different mechanisms. The tyres can hammer or pinch the stone, and in the process the stone can be deviated by some asperity on the road. Finally, the tyre tread grooves could throw stones upwards. The tread of a tyre is typically a few millimetres in width. Table 1 shows the variables and attributes of the stone impact phenomenon [8].

Table 1 - Stone impact phenomenon

Variables	Attributes
Projectile	Shape, mass, density and material constants (modulus, Poisson's ratio)
Impact conditions	Velocity and angle of incidence
Ambient conditions	Temperature and humidity
Component system	Type (material properties), thickness (injection moulding), stiffness (ribbing), strain rate properties, moisture uptake

The characteristics of stones likely to cause damage into the engine oil pan presented in the Figure 1 were quantified allowing the measurement of road stones typical mass and size [9]. The granite stones shown in Figure 2-a weigh less than 17 g and all fit into the damaged area between two consecutive ribs except the two big stones on the right side; the rounded stone weighs 21 g and the larger one weighs 78 g. There are variable gaps between the ribs in the area of impact. An 87 g random stone with a pointy profile is able to fit into the gap where damage is evident, Figure 2-b. A possible solution would be to reduce the rib spacing so as to exclude more stones, Figure 2-c. However, the mistake would be to overload the oil pan structure with protective features. The compromise is in the balance in where more or improved ribs are disposed in the areas prone to impacts.

 a  b  c

Figure 2 - Collection of random stones

2. Experimental testing

2.1 Materials and manufacture of oil pan samples

Two commercial grades of polyamide 66 with 35 wt% of short discontinuous glass fibre, Ultramid A3HG7 (PA66-GF35) and Ultramid A3ZG7 (rubber toughened PA66-GF35) were manufactured by BASF. The rubber modifier in the rubber-toughened material has been intimately melt-blended into the base material. Previous studies have shown that one of the most promising types of elastomers used as toughening agents for polyamides are EPR copolymers in addition of about 20 wt% in the form of small particles [10-15]. The polyamides are copolymerised with the EPR chains on the terminal amine groups of the polyamide. The graft copolymers produced aids dispersion, creating separate phases in the solid enhancing interfacial adhesion. The glass fibres have an average length (l) of 300 μm and diameter (d) of 13 μm, thus yielding an average aspect ratio (l/d) of 23. The materials are initially extrusion compounded into pellets by dry blending glass fibres with PA66 pellets and then are injection moulded into oil pans. The process cycle of injection moulding consists of four stages: clamping, injection, cooling and ejection. The cycle begins when the clamping unit closes the mould halves together. Next, the granulated PA66 is melted with chopped glass fibres by heat between 280-300°C (above its melt temperature of 260°C) and pressure around 100 bars. The molten plastic is then injected with a screw at 200-300 mm/s into the mould cavity (mould temperature 80-90°C). When the mould is filled, a holding pressure is

maintained to compensate for the volumetric contraction occurring (shrinkage 0.5%) on solidification and subsequent cooling. After cooling, the part is ejected from the mould [16]. All test samples in this study come from the same batch of material and are henceforth named PA66-GF35 (A3HG7) and PA66-i-GF35 (A3ZG7) for the toughened material.

The design of the oil pan is made in such a way that its connection to the engine is consistent with the metal construction previously used. A distinguishable element of the design is the ribbing pattern which provided increased stiffness. Ribs are part of the oil pan and are not meant to snap, however, damage such as crushed or deflected ribs are acceptable at high impact energy. Figure 3 shows an early version of the oil pan made with PA66-GF35. This oil pan weights around 2.4 kg. Overall dimensions are 580 × 300 × 75/160 mm. Thickness of the base wall is 3 mm. Ribbing heights varies from 6-20 mm, ribbing thickness is 2 mm, rib spacing varies from 5-30 mm.

Figure 4 shows the last improved version of the oil pan made with PA66-i-GF35. This oil pan weights around 2.6 kg. Overall dimensions are 580 × 300 × 60/200 mm. Thickness of the base wall is 3 mm. Ribbing heights varies from 10-20 mm, ribbing thickness is 2 mm, rib spacing varies from 5-15 mm.

Figure 3 - Early version of the oil pan

Figure 4 - Improved version of the oil pan

2.2 Mechanical testing and conditions

Experimental impact tests are carried out using a drop weight tower and a gas gun. The drop weight tower has been conducted by adjusting the height of a 10 mm hemi-spherical tip impactor (3170 g total falling weight, boulder impact scenario) to the desired impact energies. Gas gun impact tester employs a 10 mm hemi-spherical 22 g projectile (flying stone impact scenario) and has been conducted by adjusting the pressure in the gun to reach the desired impact velocities. The two experimental methods (guided drop tower and projectile) were used. The drop tower provides more impact information but the impactor is constrained during the falling and has only one degree of freedom. The projectile method gives limited impact information but since it is a projectile, it is more representative of a stone impact. The projectile and impactor were chosen according to the collection of random stones presented in Figure 2. A picture showing side-by-side, projectile, impactor and reference stone was provided in Figure 5.

Figure 5 - Road stone, projectile and impactor

Single impacts of energy range from 3-12 J at 90° to surface (giving maximum impact energy to the wall of the part) at room temperature are investigated. Impact energies, for the reference stone or projectile, represent a driving speed from 50-120 km/h. Targeted positions are all

around the oil pan, on flat walls, on ribs and between, and on groove walls. Each position has been impacted 10 times on 10 different samples. Oil pans are tested bolted on steel plate and clamped to the test fixture. The tested oil pans did not contain oil or welded part during the testing. Impact resistance specifications are 7 J for sidewalls (likely to be impacted to an oblique angle, with less impact energy transferred) and 12 J for bottom walls facing the road (likely to be impacted to an angle of 90° with maximum impact energy transmitted to the wall).

Broken off fragments of the oil pan during testing were examined under Scanning Electron Microscope (SEM) to observe fracture mechanisms.

3. Finite element analysis

Simulation impacts on the oil pan were conducted using experimental data. Early design model (80468 shell elements) and improved design model (118205 shell elements). Thickness of the part is 3 mm for the wall and 2 mm for the rib. Models are constrained in all directions on their sealing edges.

The oil pan models were meshed using HyperMesh from Altair HyperWorks 9.0 with LS-DYNA interface. Once the geometries are ready, the pre-processing begins assigning sections, materials properties and configuring behaviours, interactions and boundary conditions in the environment. The pre-processing was completed with LS-PrePost 2.4 whilst the simulations were processed with LS-DYNA solver version 970 both from LSTC. LS-DYNA was selected for its analysis capabilities (non-linear dynamics, failure analysis, crack propagation and more) and also its comprehensive library of materials models and contact algorithms. LS-PrePost 2.4 was also used to complete the post-processing analyses.

The simulations are based on the stress-strain relations obtained from the experimental work with fixed conditions to describe a specific situation. The representation of the material uses elasto-plastic material law [17-18]. The elastic Young's modulus defines the stress-strain relation up to the yield stress. Above yield stress, the plastic behaviour is described by effective stress and effective plastic strain coordinates. The material failure is set using strain failure criterion. If the calculated effective plastic strain for any

element exceeds the predefined value, the element is removed from the model and the simulation continues with the eroded model. If the strain rate increases the failure strain drops but the model understands that this parameter is constant and independent. Therefore, this failure criterion is updated and varies in correlation with the strain rate.

4. Results and discussion

Figure 6 shows the early version of the PA66-GF35 oil pan with key areas highlighted. Gas gun tests results are:

- Areas in (A) are covered with flat walls, groove walls (25 mm diameter) and walls with Y-axis ribs (spacing 10 mm, height 6 mm). Areas in (A) must resist to a 7 J impact. However, 80% of flat walls failed at 3 J because walls are directly exposed; 100% of groove walls failed at 3 J because concave shape are fragile and uncovered; and 60% of walls with Y-axis ribs failed at 7 J with damaged ribs because impacts between ribs can be directly reached by the projectile.
- Bottom walls in (B) are covered with ribbing mesh pattern (Z-axis ribs height 10 mm, spacing 15 mm; X-axis ribs height 5 mm, spacing 25 mm). Areas in (B) must resist to a 12 J impact. However, in the low density ribbing area 60% of walls failed at 12 J because of rib spacing too large; and in the high density ribbing area 20% of walls failed at 12 J at the bottom of the rib.
- Walls in (C) are represented by Y-axis ribs, flat and groove walls. Areas near the pick-up oil channel feature must resist 7 J but 40% of walls failed especially nearby uncovered sharp angles. Areas near the cylinder feature must resist 12 J but 80% of walls failed because of uncovered concave walls, tall ribs easily snapped and a lack of dense ribbing pattern. Transitions between areas (C) and (B) are at 90° and characterise zones of stress concentration.
- Walls in (D) are covered with Y-axis ribs (spacing 15 mm) and groove walls. Area in (D) must resist 7 J. However 60% of ribbed walls failed because of rib spacing too large; 80% of groove walls failed because of uncovered concave walls.

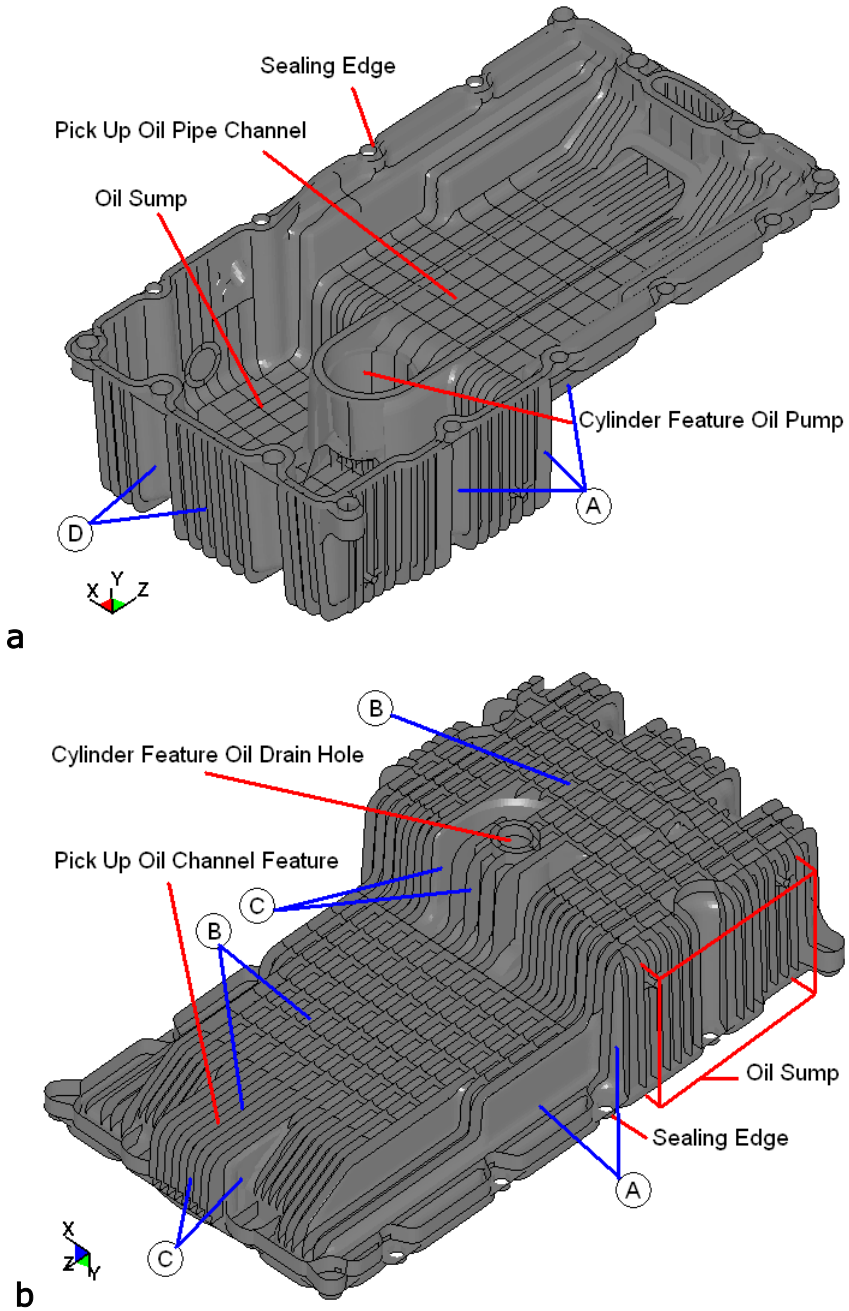

Figure 6 - Early version of the oil pan and key areas, a) inner view, b) outer view

Impact resistance results of the early version of the oil pan are rather alarming. Figure 7 and Figure 8 show typical failures encountered in each area. Figure 7 displays crack failures in Area A, impact between two ribs, and in Area D, impact in a concave groove wall. Figure 8 displays broken ribs

and perforation in Area B and crack (sharp junction between surfaces) and perforation (concave cylinder feature) in Area C. Almost all causes of failure were taking place on exposed areas, on unprotected walls and where the rib spacing is too large. Other failures were spotted on sharp transitions between surfaces resulting in long scale cracks along the separating line between each surface. Finally, 95% of ribs higher than 15 mm were snapped. Tall ribs are not enough stiff, they are deflecting too much which cause the removal of long portion of ribs whilst impacted. 90% of failures were cracks, 75% of them were only visible on the inner side of the oil pan and 15% were visible on both side of the wall. The rest 10% were perforations of the wall.

Area A

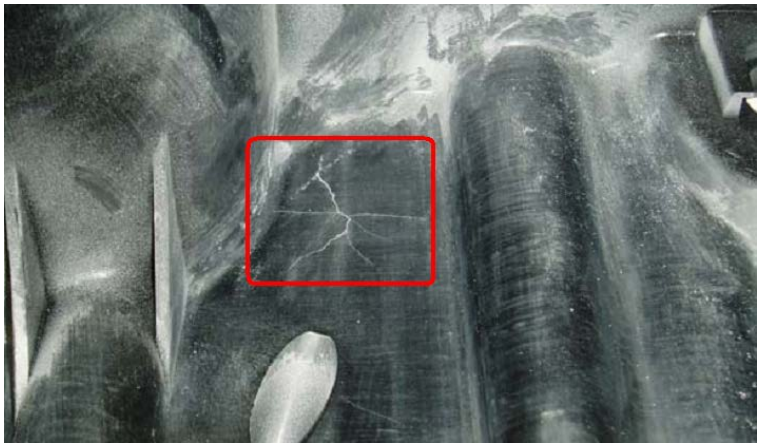

Area D

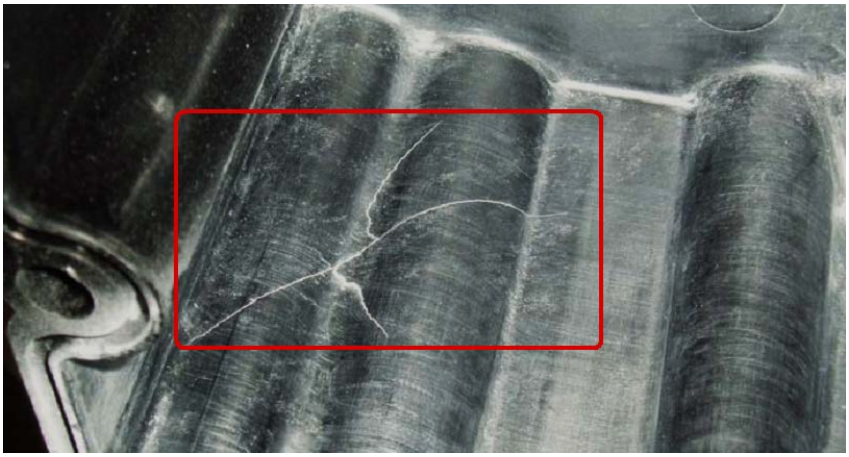

Figure 7 - Typical failures encountered in Area A (7 J) and Area D (7 J)

Area B

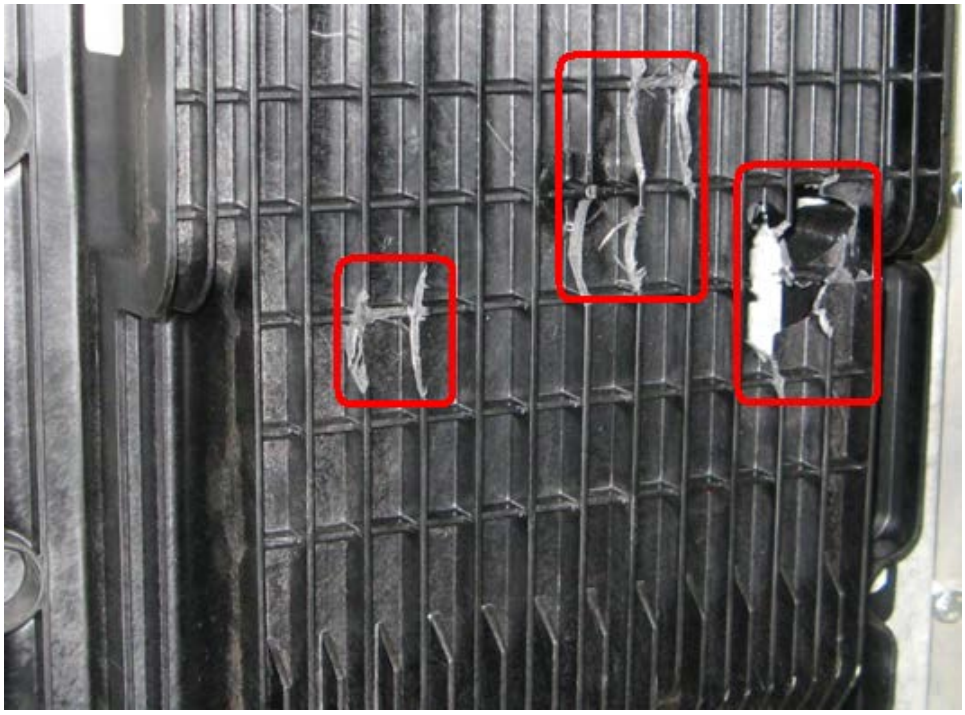

Area C

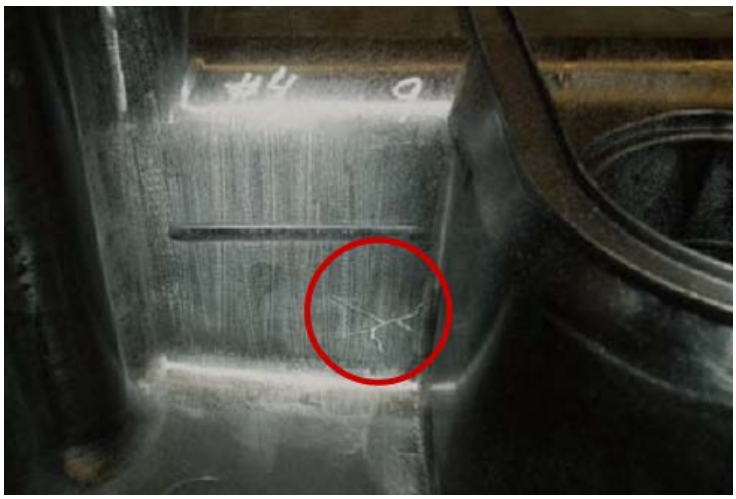

Figure 8 - Typical failures encountered in Area B (12 J) and Area C (12 J)

A broken off fragment from the Area B (PA66-GF35) was put under SEM observation. The magnitude of the following Figures varies from 200-4000. In Figure 9, the two constituents characterising the composite are clearly distinguishable that is to say short glass fibres and matrix resin wrapping the fibres. The picture reveals that there is a wide range of fibres

pointing in a general direction, the direction of the injection moulding flow (skin area). At magnitude of 200, fibres mostly appear entire (average length of 300 μm), some are uncoated but they seem unaltered whilst the matrix is unevenly distributed with some bits peeled or detached. Besides, fibres emerging from the fractured surface have been displaced and are completely de-bonded from the matrix precisely because of a lack of matrix. Unmistakably, it is a sign of a matrix cracking failure.

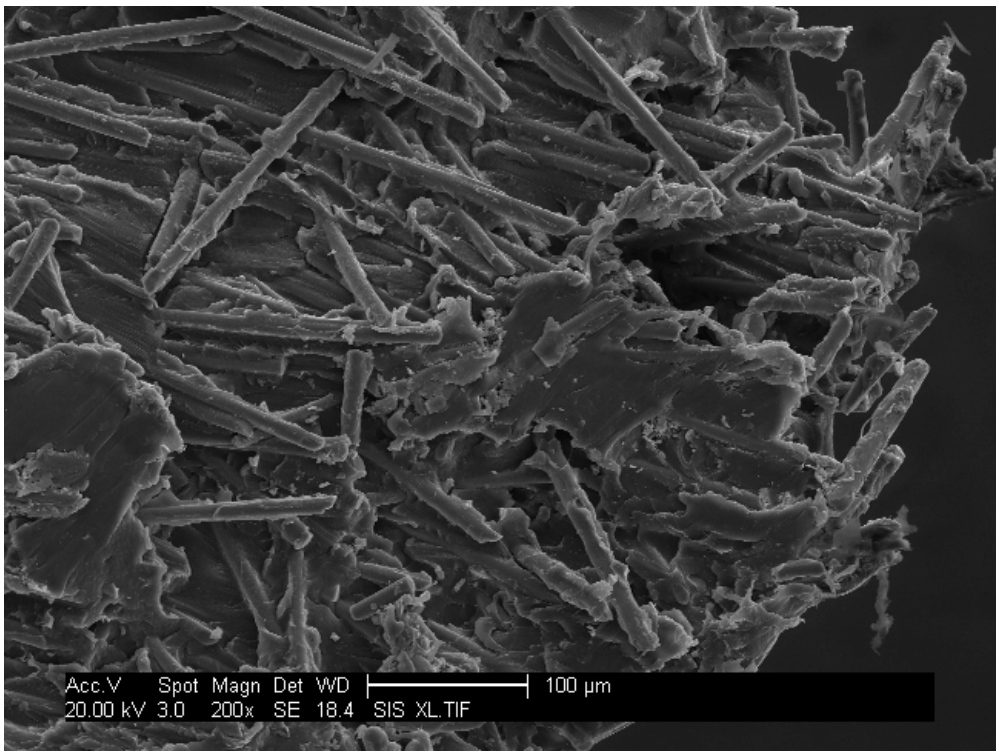

Figure 9 - Matrix cracking failure at magnitude 200 (Area B, 12 J)

When the area towards the centre of the fragment is magnified, we stumble upon other type of breaks, but they are still localised in the impact point area. At magnitude of 400, Figure 10 shows failures surrounding the impacted surface. Both matrix and fibres have failed. The picture illustrates a net cut section of each material constituent. In this area, compression stress acted more than tension stress. Fibres are shorter than normal (<50 μm) and are also randomly dispersed (core area). They are also few holes and hollows caused by fibres pulling out of the matrix but for the major part, matrix and fibres remained linked together.

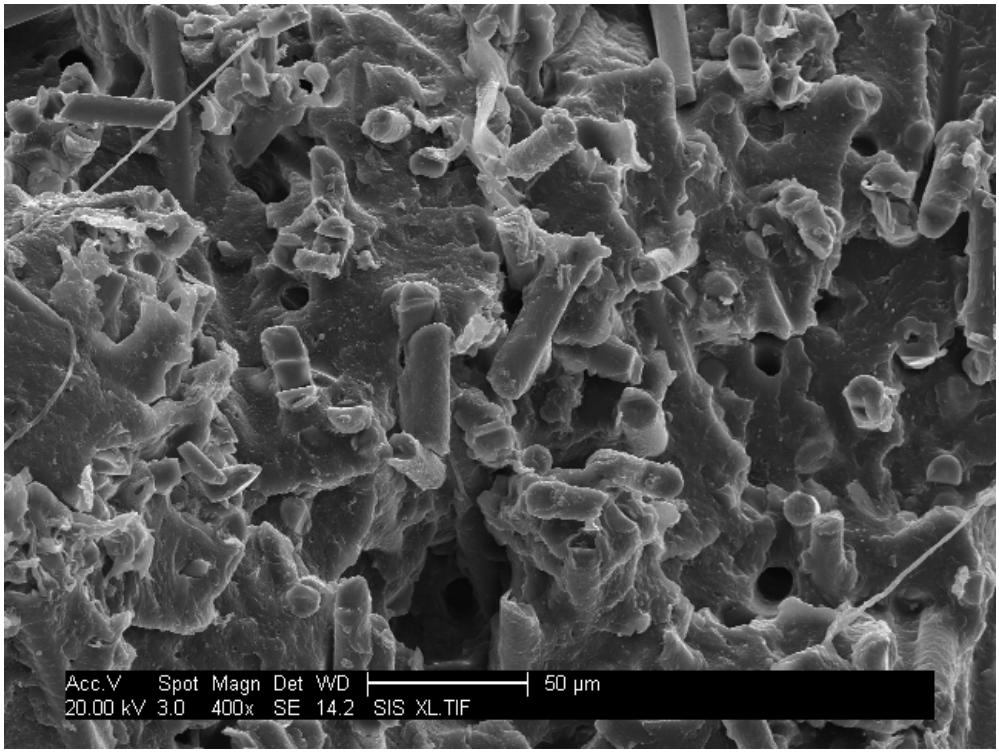

Figure 10 - Matrix cracking, fibres fracture and limited fibres pull out at magnitude 400 (Area B, 12 J)

At the same magnitude of 400, Figure 11 shows failures taken from the backside of the impacted surface. Many hollows are visible from where fibres were filling them and also many uncoated fibres can be spotted. In this region of the fractured surface, the bond between fibres and the matrix has yielded first. This upshot illustrates the fact that in this area of the sample tension stress is bigger than compression stress. The system de-bonds and fibres are pulled out of the matrix during the fracture. Noticeably, the matrix has failed in its function. Fibres seem to have a general direction which confirms that the area is in the skin section of the sample (skin-core morphology during injection moulding).

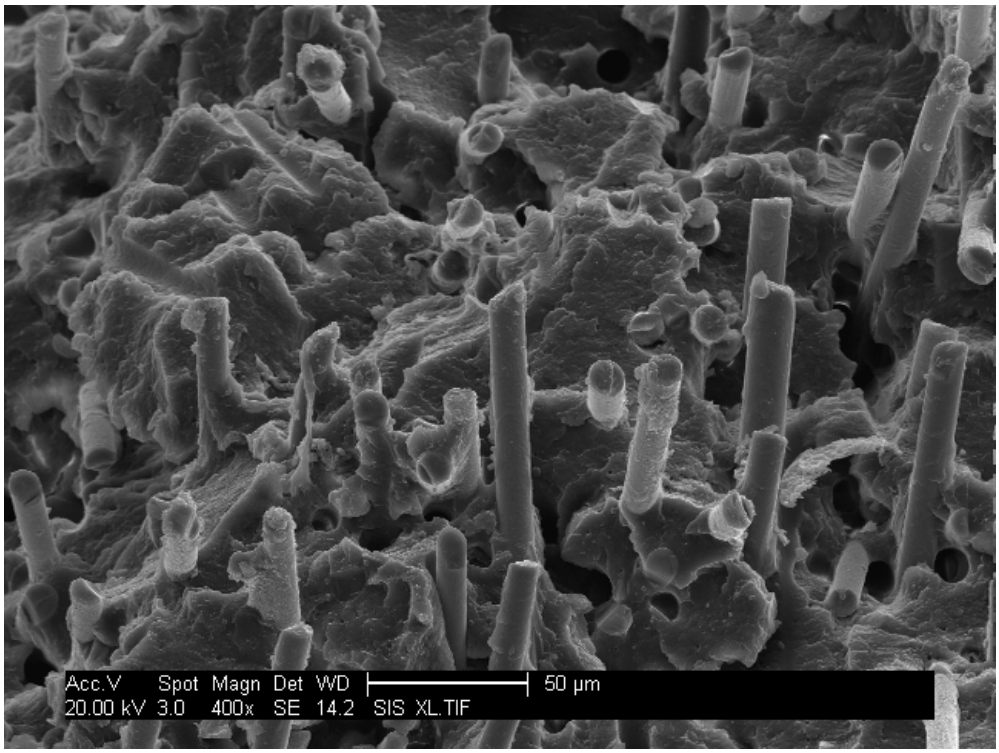

Figure 11 - De-bonded and pulled out fibres at magnitude 400 (Area C, 12 J)

Figure 12 shows one end of a fibre which presents a tear on its surface probably resulting from a failure across the diameter of the fibre. The fractured fibre was perpendicular and in line with the general direction of the impact. The stress was so intense that it has removed the matrix and split the fibre in two with a peeled chip still attached to the fibre. Chopped fibres in their major part present a bevel-shaped fracture. For a matter of comparison, another fibre is visible at the bottom background that presents a clean flat end surface. Furthermore, the base of the matrix where the ruptured fibre is attached displays also a fissure.

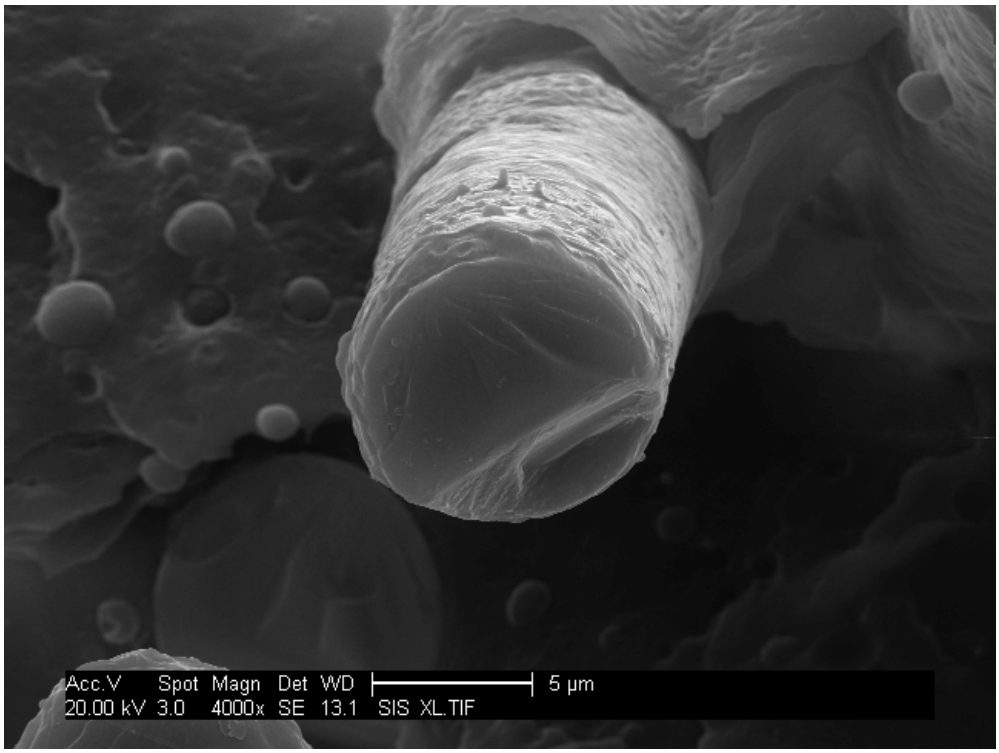

Figure 12 - Close-up of a fibre fracture at magnitude 400 (Area C, 12 J)

Figure 13 shows the latest improved version of the PA66-i-GF35 oil pan with key areas highlighted compared to the early version. Gas gun results are:

- Areas in (A) that were found weak received improvements. Flat walls are now covered with Y-axis ribs spaced by 8 mm (10 mm from the centre of each rib). Groove walls are reinforced by layered ribs from 10-5 mm in height around them. The pattern of ribbed walls was made denser with rib spacing of 8 mm and height of 10 mm. At 7 J, the only damage observed was crushed ribs by 2 mm maximum.
- Bottom walls in (B) received a denser ribbing pattern with homogeneous rib height of 10 mm (rib spacing in Z-axis is now 8 mm and 15 mm in X-axis). At 12 J, the base wall was never directly touched and no visible cracks were found.
- The main improvement in areas in (C) concerned the transition between the sump and the pan especially at the bottom transition. Instead of being at 90° which were zones of stress concentration, they

are now presenting a smooth rounded transition. This chamfer allows a better distribution of the effort in a much wider surface area. Another chamfer or recess was introduced on the transition edges to accommodate the height difference. The cylinder feature found in the previous design was extremely weak with large rib, large spacing and unprotected concave grooves. It was removed and the oil drain hole was moved off-centred to a position where it was feasible to integrate it. The pick-up oil channel is not straight anymore and has an S-shape look in accordance with the move of the drain hole. The other improvements are similar to areas in (A). No wall is left uncovered and Y-axis ribs were increased in density around grooves. The transition between sump and pan contains two X-axis ribs across the denser Y-axis ribs (spacing 8 mm). This was intended to reduce the broken-off fragments of ribs. At 7 J, no failure is visible, only marks, scratches or small crushes (1-2 mm). At 12 J, some Y-axis ribs are likely to be crushed (by 2-3 mm) but again no failures are observed.

- Walls in (D) received same improvements as in (A). Reduction of the rib spacing (8 mm), Y-axis ribs height to 10 mm, and grooves protected with layered ribs (10-5 mm height).

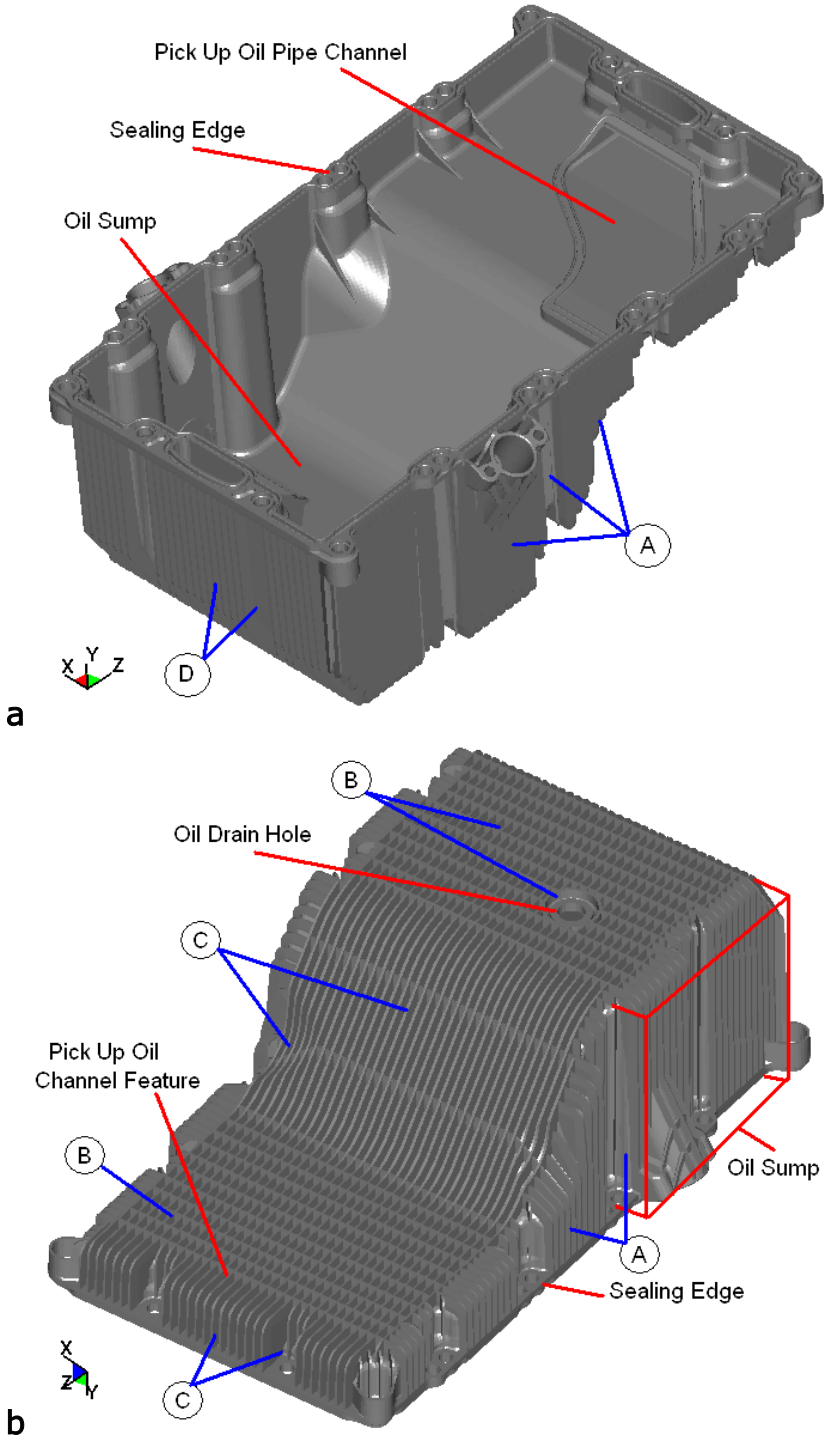

Figure 13 - Improved version of the oil pan and key areas, a) inner view, b) outer view

Figure 14 shows forces histories of each structure impacted at 3 J (drop tower) in the middle of a rib spacing in Area (B) on the pan section. In the early version, Z-axis ribs height is 10 mm and X-axis ribs height is 5 mm; spacing between Z-axis ribs is 15 mm and between X-axis is 25 mm. Therefore a 10 mm surface impact directly hits the wall. In the improved version, Z-axis and X-axis ribs heights are 10 mm and spacing between Z-axis ribs is 8 mm and between X-axis ribs is 15 mm. Consequently, a 10 mm surface impact inevitably hits the ribbing. The 3 J impact on the early version can be described as follows, between 0-3 ms, the wall deflects. At 3 ms, the maximum deflection is reached for the given impact. From then, the wall pushes back the impactor. The 3 J impact on the improved version has a different scenario. The impactor touches the two Z-axis ribs which resist and slightly deflects till 2.4 ms. From then, ribs deflect and the impactor slightly penetrates in between thus the fall in the force. At 2.6 ms, ribs start to stop deflecting and at 3 ms the walls of the ribs begin to push back the impactor. The oscillation in the force can be interpreted by successive returns between each rib wall. At 3 J, no failure is observed on each structure.

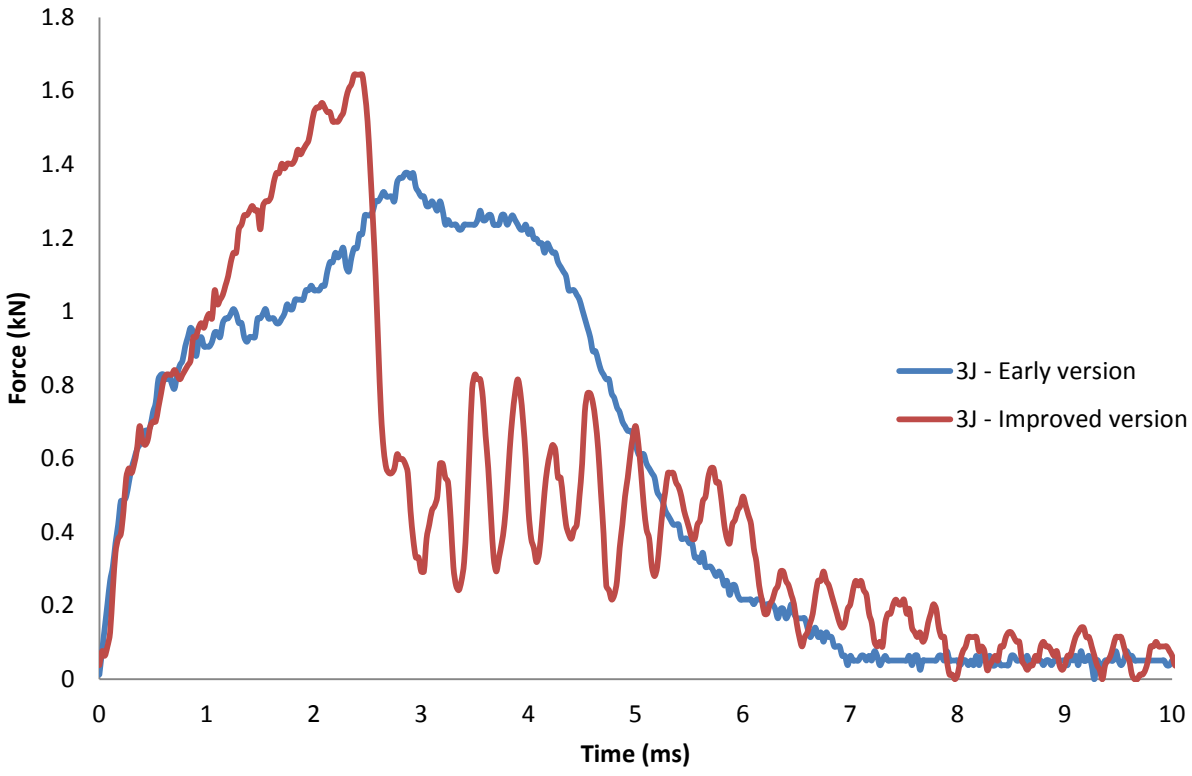

Figure 14 - Forces histories for each design at 3 J

Figure 15 shows forces histories of each structure impacted at 7 J (drop tower) in the same area as before but on a blank spot of impact. In the 7 J impact on the early version, the wall deflects and begins to show signs of damage at 2.4 ms till it eventually fails at 3.5 ms. Crash appeared on both sides of the wall. In the 7 J impact on the improved version, the two ribs are successively touched and crushed till their walls stop to crush at 0.75 ms. From then, they resist, deflect and push back the impactor. No failure is visible on the wall but only damaged ribs. Figure 16 illustrates an example of a 3 mm crushed rib on the pick-up oil channel feature.

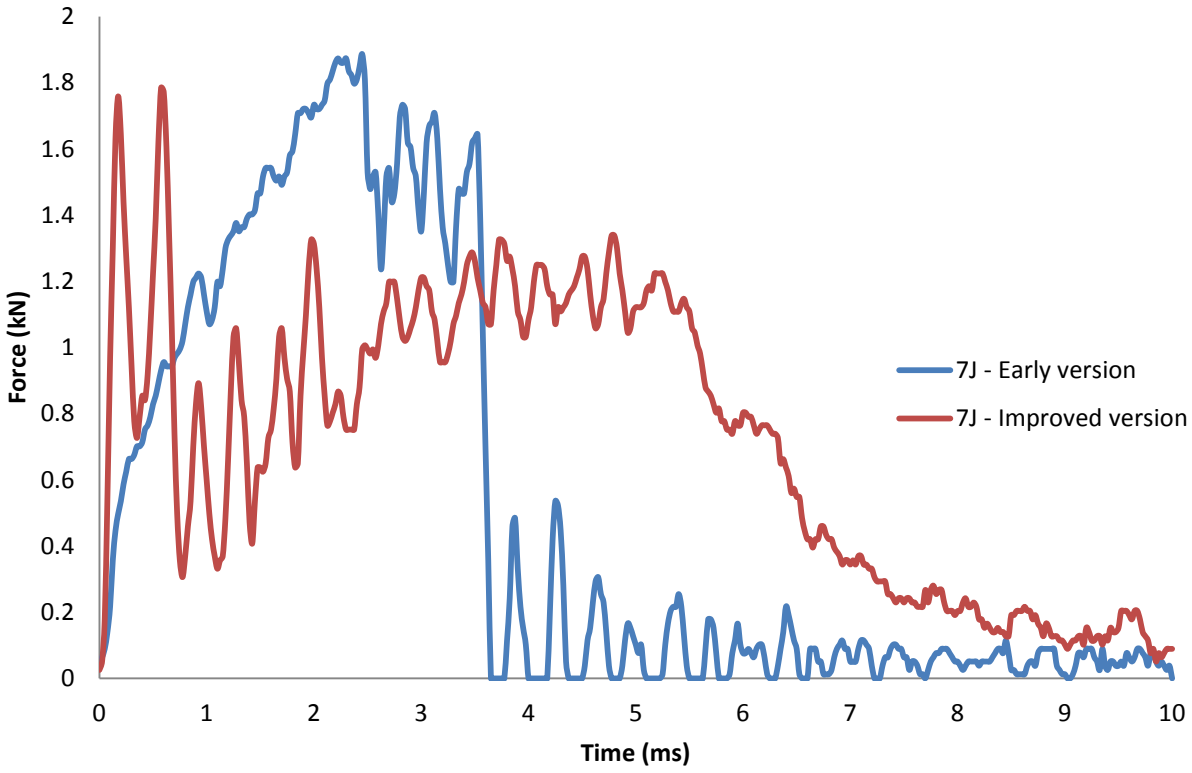

Figure 15 - Forces histories for each design at 7 J

Figure 16 - Rib crushed after impact on rib at 7 J (PA66-i-Gf35)

Figure 17 shows the correlation between 7 J experimental and simulated impacts on the same location of the improved version (PA66-i-GF35). The general look of each curve appears similar. However, forces in the model are overestimated at the beginning of the impact and underestimated towards the end. The model predicts around 20% more strength (2.15 kN instead of 1.76 kN) when the impactor tries to penetrate between the ribs and around 60% less towards the end (0.5 kN instead of 0.8 kN). However, the order of magnitude is correct and the model can be used to approximate the impact behaviour of the oil pan.

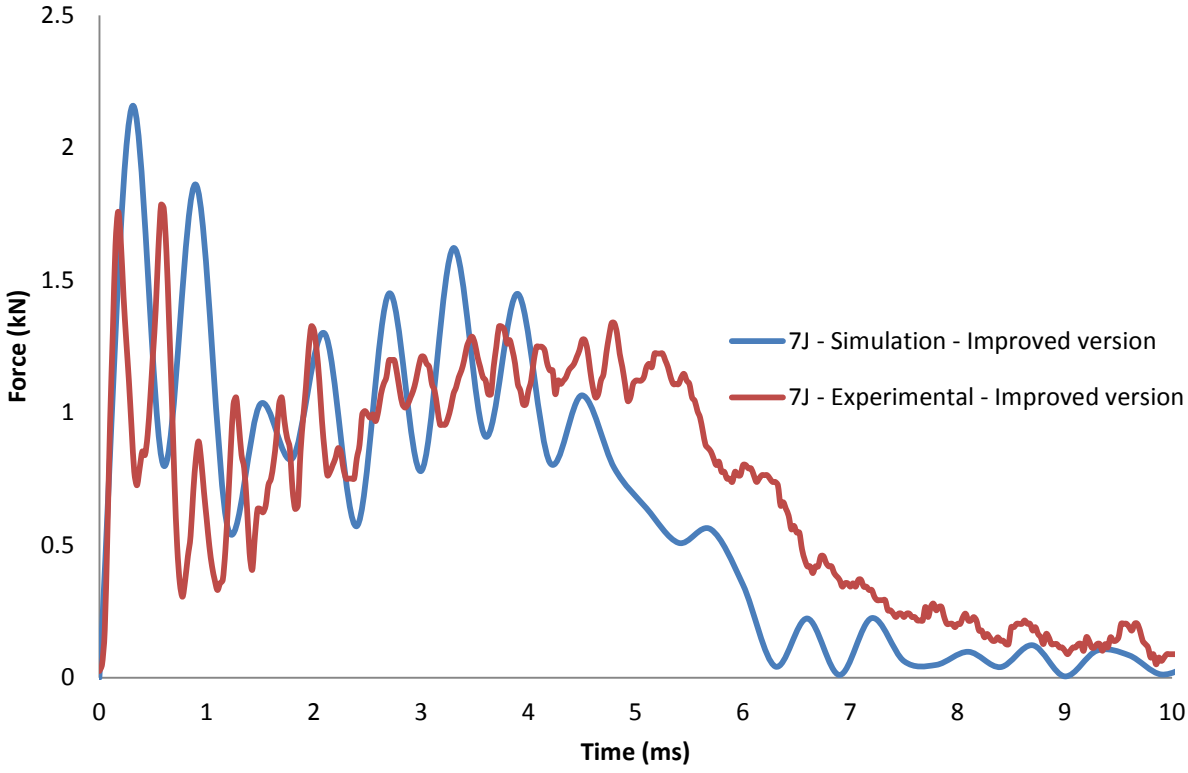

Figure 17 - Experimental and simulation forces histories on improved design at 7 J

Figure 18 shows a 10 mm projectile impact sequence at 14 m/s with shock waves stress distribution propagating in circle away from the impact spot. At t_2 when shock waves reach sharp edges, an accumulation of stress is created. The impact occurs in the base wall and the ribbing restrains the wall to deflect to a certain extent. The ribbing plays a major role in the stress distribution [19-20].

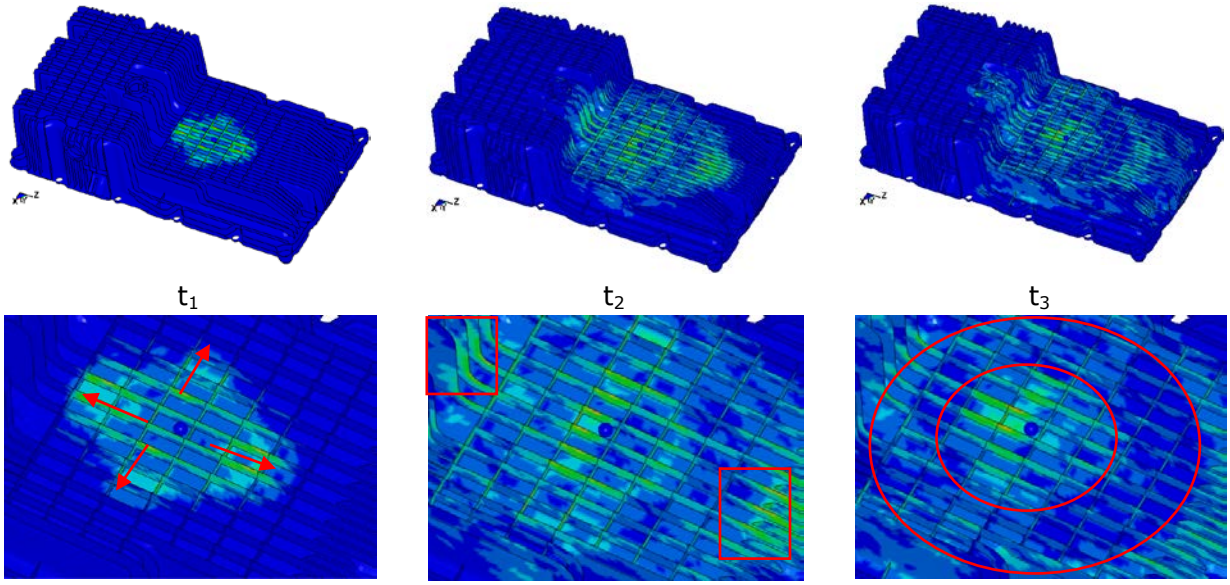

Figure 18 - Evolution of the stress undergone by the oil pan structure

5. Conclusions

Impact performance were realised on different oil pan design. Investigations of weak areas of the early version were identified such as, sharp surface transition which are stress concentration zones, unprotected areas displaying the base wall (concave grooves, flat walls), the oil cylinder feature which presents sharp angles, unprotected walls and tall ribs. From then, improvements were added on the design which led to the latest version. The improvement of the design was taking into account different

elements of the engine surrounding the oil pan. Sharp angular surface transitions are made rounded. The oil cylinder feature was removed and the oil drain hole moved to possible relocation. Therefore the transition between the sump and the pan is made with the same wall which also received stiffening rib lines. The surface transition between sump, pan and their respective side walls are accommodated by creating a curved recess on the edge. Uncovered walls needed protective ribbing feature. The reduction of the rib spacing or densification of the ribbing led to higher impact performance. The standardisation on the rib height permitted better distribution of the impact. In terms of materials, the toughness of PA66-i-GF35 allows more progressive deformation or damage of ribs (crushing) instead of brittle behaviours of PA66-GF35 ribs which were easily broken up. The improvement on the latest version of the oil pan did not show a sign of failure on the base wall. Impact simulations were found to give good correlations with impact experiments. However, when the impact induces material response close to its yielding point, the outcome can be slightly over or underestimated by 10-15%. Nevertheless, it was found as well in the experiments that the yield on the structure has to be considered with a 0.5-1 J margin. Therefore specifications were taking this parameter into account.

SEM analysis on PA66-GF35 showed that fibre-matrix interface rupture is observed. The damage is characterised by matrix plastication, matrix micro-cracks, fibre pull out and fibre fracture. Localised impact against the composite wall acts like a dynamic flexion with characteristic tension failure on the backside and compression failure on the impacted side. Once the projectile enters in contact with the wall, the wall quickly starts to undergo deformation, bends and eventually fails if the impact intensity is higher than the wall can cope. The excess of energy in the structure is evacuated through tension stresses that make the matrix to crack and the interfacial to break. Cracks were always found initiated on the backside of the impacted wall and can propagate towards the impacted side if the impact energy is sufficiently important.

Acknowledgment

The authors gratefully acknowledge the financial support from both the EPSRC grant CASE/CAN/07/40 and Research Council UK. Z.Mouti would also to thank EATON for financial support on current research program at Cranfield University whose results are reported in this work. The authors also wish to acknowledge SABRE BALLISTICS for their support on gas gun testing and useful discussions.

References

[1] Nguyen, S. N., Greenhalgh, E. S., Olsson, R., Lannucci, L. and Curtis, P. T. (2010), "Parametric analysis of runway stone lofting mechanisms", *International Journal of Impact Engineering,* vol. 37, no. 5, pp. 502-514.

[2] EA R&D Avalon Field Test Cummins (2008), *Oil Pan Crack Failure*.

[3] Pacejka, H. B. (ed.) (2006), *Tyre and Vehicle Dynamics,* Elsevier/Butterworth-Heinemann, Amsterdam/London.

[4] Nguyen, S. N., Greenhalgh, E. S., Olsson, R., Lannucci, L. and Curtis, P. T. (2008), "Modeling the Lofting of Runway Debris by Aircraft Tires", *Journal of Aircraft,* vol. 45, no. 5, pp. 1701-1714.

[5] Nguyen, S. N., Greenhalgh, E. S., Lannucci, L., Longstaff, S., Olsson, R. and Curtis, P. T. (2011), "Experimental Characterisation of Tyre Indentation by Simulated Runway Debris", *Strain,* vol. 47, no. 4, pp. 343-350.

[6] Longstaff, S. (2008), *Experimental characterisation of the interaction between tyres and stones* (Final Year Project (M.E.) thesis), Department of Aeronautics, Imperial College, London.

[7] Mines, R. A. W., McKown, S. and Birch, R. S. (2007), "Impact of aircraft rubber tyre fragments on aluminium alloy plates: I –

Experimental", *International Journal of Impact Engineering,* , no. 34, pp. 627–646.

[8] Ramamurthy, A. C., Lorenzen, W. I. and Bless, S. J. (1994), "Stone impact damage to automotive paint finishes: An introduction to impact physics and impact induced corrosion", *Progress in Organic Coatings,* vol. 25, no. 1, pp. 43-71.

[9] Mouti, Z., Westwood, K., Kayvantash, K. and Njuguna, J. (2010), "Low Velocity Impact Behavior of Glass Filled Fiber-Reinforced Thermoplastic Engine Components", *Materials,* vol. 3, no. 4, pp. 2463-2473.

[10] Flexman, E. A. (1979), "Impact behavior of nylon-66 compositions: Ductile-brittle transitions", *Polymer Engineering & Science,* vol. 19, no. 8, pp. 564-571.

[11] Bucknall, C. B., Heather, P. and Lazzeri, A. (1989), "Rubber toughening of plastics", *Journal of Materials Science,* vol. 24, no. 6, pp. 2255-2261.

[12] Borggreve, R. J. M., Gaymans, R. J., Schuijer, J. and Housz, J. F. I. (1987), "Brittle-tough transition in nylon-rubber blends: effect of rubber concentration and particle size", *Polymer,* vol. 28, no. 9, pp. 1489-1496.

[13] Cimmino, S., D'Orazio, L., Greco, R., Maglio, G., Malinconico, M., Mancarella, C., Martuscelli, E., Palumbo, R. and Ragosta, G. (1984), "Morphology - Properties Relationships in Binary Polyamide 6/Rubber Blends: Influence of the Addition of a Functionalized Rubber", *Polymer Engineering and Science,* vol. 24, no. 1, pp. 48-56.

[14] Willis, J. M. and Favis, B. D. (1988), "Processing-morphology relationships of compatibilized polyolefin/polyamide blends. Part I: The effect of an lonomer compatibilizer on blend morphology", *Polymer Engineering & Science,* vol. 28, no. 21, pp. 1416-1426.

[15] Wu, S. (1983), "Impact fracture mechanisms in polymer blends: Rubber-toughened nylon", *Journal of Polymer Science: Polymer Physics Edition,* vol. 21, no. 5, pp. 699-716.

[16] BASF SE (2011)*, Processing by injection molding*, available at: http://www.plasticsportal.net/wa/plasticsEU~en_GB/portal/show/common/content/products/engineering_plastics/ultramid/processing_by_injection_molding.

[17] Lobo, H. and Hurtado, J. "Characterization and Modeling of Nonlinear Behavior of Plastics", *ABAQUS User Conference*, 2006, Boston, USA.

[18] Lobo, H. "Methodology for Selection of Material Models for Plastics Impact Simulation", *10th International LS-Dyna User's Conference*, 2006, Detroit, USA.

[19] Mouti, Z., Westwood, K., Long, D. and Njuguna, J. (2011), "Finite element analysis of localised impact loading on short glass fibre-reinforced polyamide engine oil pan subjected to low velocity impact from flying projectiles", *8th European LS-DYNA Users Conference,* May 2011, Strasbourg, France .

[20] Hasenauer, J., Küper, D., Laumeyer, J. E. and Welsh, I. *Top Ten Design Tips - A Series of 10 Articles*, DuPont, 2007.